A Fired Silicon-based Heterojunction (FlaSH) passivating contact for next generation industrial c-Si solar cells

Andrea Ingenito[1], Gizem Nogay[1], Quentin Jeangros[1], Esteban Rucavado[1], Christophe Allebé[2], Santhana Moorthy[3], Nathalie Valle[3], Tom Wirtz[3], , Jörg Horzel[2], Takashi Koida[4], Monica Morales Masis[1], Matthieu Despeisse[2], Franz-Josef Haug[1], Philipp Löper[1], Christophe Ballif[1,2]

[1] *École Polytechnique Fédérale de Lausanne (EPFL), Institute of microengineering (IMT), Photovoltaics and Thin Film Electronics Laboratory, Rue de la Maladière 71b, CH-2000 Neuchâtel, Switzerland*

[2] *CSEM PV-Center, (CSEM), Rue Jaquet-Droz 1, CH-2002 Neuchâtel, Switzerland*

[3] *Luxembourg Institute of Science and Technology, Advanced Instrumentation for Ion Nano-Analytics (AINA), Materials Research and Technology Department, 41, rue du Brill, L-4422 Belvaux, Luxembourg*

[4] *Research Center for Photovoltaic Technologies, National Institute of Advanced Industrial Science and Technology (AIST), Central 2, Umezono 1-1-1, Tsukuba, Ibaraki 305-8568, Japan*

Abstract:

As highlighted by recent conversion efficiency records, passivating contacts are keys to fully exploit the potential of crystalline silicon as a light absorbing semiconductor. Prime passivating contact technologies include a-Si/c-Si silicon heterojunctions and high temperature tunnel oxide/polysilicon-based contacts. The first has the advantage of a simple fabrication process, but it is incompatible with standard metallization processes and bulk semiconductor defect treatments which take place at temperature > 800°C. The second relies on a buried junction or dopant profile near the tunnel oxide, and requires process times of several minutes at high temperature. In this paper, we solve the scientific question to know whether such a dopant profiles, with the possible the presence of nano-holes, is required to make an efficient contact when using a tunnel oxide. We show that, by leveraging the versatility of plasma deposition processes, it is possible to realize Si-based thin-film doped layers that withstand a short annealing at high temperature (> 800 for typ 10 s, called "firing"), passivate the c-Si interface and foster collection of photo-generated charge carriers by inducing a strong electric field at the Si-surface near the interface with SiO_x. The contact has a high-compatibility with existing industrial process: a plasma deposition of a thin-film layer at the rear side followed by a rapid thermal treatment ("firing"), an essential process for metallization formation of industrial cells. With the developed technology, we fabricated proof-of-concept p-type solar cells with conversion efficiency up to 21.9%.

1. Introduction

Solar photovoltaic (PV) power was the fastest-growing energy source in 2016 and 2017, and for the first time, the newly installed solar PV capacity exceeded the growth of any other form of power generation[1]. Wafer based crystalline-silicon (c-Si) solar cells own the largest share in the photovoltaic (PV) market (> 90%) and will likely keep their dominant role in the near and midterm future[2]. Improving the energy-conversion efficiency of solar cells directly reduces their costs, thus offering a valuable route to improve cost-competitiveness of solar PV power with respect to other energy sources. For industrial c-Si solar cells extraction of photo-generated carriers is provided by metallic contacts made of screen-printed pastes, Ag-grid and Al on front the rear side respectively, followed by a fast firing (T>700°C; <10s). As result, the Ag-based paste etches-through a SiN_x:H, used as antireflection coating, while on the rear side a full-area Al back surface field (Al-BSF) is formed, giving the name to this cell architecture. Charge carrier recombination due to direct contact between metal and Si represents a major efficiency-limiting factor for industrial c-Si solar cells[3,4]. To mitigate such losses, industrial Al-BSF cells rely

on heavily-doped Si regions which lower the density of minority charge carriers available for recombination at the highly-defective Si-metal interface. Aside doping, contact recombination can be further reduced by restricting the metallized area. Technologically, this is achieved by using a patterned dielectric passivation layer forming a partial rear contact (PRC). This concept is applied in passivated emitter and rear cell (PERC) architecture that is being widely adopted at industrial level[2]. The charm of PERC solar cells lies in the fact that the efficiency gain is attainable, 0.8-1%$_{abs}$ over Al-BSF[2], by a merely evolutionary upgrade of existing production lines hence offering a low cost-of-ownership solution. As drawback, PRC schemes require a patterning step that increases their fabrication complexity, and they suffer from a fundamental trade-off between charge carrier transport and contact recombination[5]. Technological and physical limitations of traditional approaches for reducing contact recombination can be overcome by depositing, on Si, thin-films that passivate surface defects and provide charge carrier extraction at the same time (i.e. passivating contacts). A prime example of passivating contacts is the silicon heterojunction (SHJ) as highlighted by the recent world record conversion efficiency of 26.7%[6]. However, as the passivation quality of the hydrogenated amorphous silicon (a-Si:H) degrades upon exposure to temperatures above 250°C [7,8,9], and dedicated back-end and interconnection processes are required. Poly-silicon (poly-Si) based passivating contacts deposited on a thin SiO$_x$, or tunnel oxide, –originally widely researched in the 80s[10]– have recently attracted a lot of attention. The charge carrier selectivity of existing poly-Si based passivating contacts is supported by a buried junction in the wafer, formed by diffusion of dopant impurities from the poly-Si layer through the thin SiO$_x$ layer during a thermal anneal at temperatures of 800-1000°C, with dwell times typically in the range of 5-15 min[11,12,13,14,15,16,17]. With this technology, record efficiency of 25.8%[18] for laboratory scale two-sided contacted cells and 26.1% for fully back-contacted solar cells have been demonstrated. Despite the superior performances of such record solar cells, their high-complexity fabrication process raises some concerns about their commercial relevance. A major repercussion of the highly-competitive PV market are limited resources for new investments. In this scenario the success story of the PERC solar cell architecture reveals that novel high-efficiency concepts can be more easily industrialized if they are conceived as an add-on to existing cell concepts. In other words, innovative approaches have to be technologically compatible with existing production lines or at least be implementable with only minor upgrades of existing production lines. To this end, we search for a novel fired silicon-based heterojunction (FlaSH) contact formed by a tunnel silicon oxide (SiO$_x$) capped with a doped silicon-based layer. Different to traditional poly-Si based passivating contact technologies, which include a long and slow thermal anneal to form deep buried junctions, the FlaSH concept employs only a firing treatment resulting in an abrupt junction with the lightly doped c-Si wafer. Thanks to the firing compatibility, the FlaSH concept could be suited as an upgrade to Al-BSF or PERC lines. Technologically, this can be achieved by a full-area deposition (i.e. patterning-free) on the rear side and co-firing with Ag-paste for contacting of the front emitter. By leveraging on the unique versatility of the plasma enhanced chemical vapor deposition (PECVD) technique, we incorporated C-atoms within the Si network in order to obtain thin doped layers that withstand firing without delamination (i.e. blistering-free) and at the same time provide good surface passivation and charge carrier transport. Here, a detailed analysis on the structural, electrical, and chemical properties of our passivating contact technology is presented. Finally, the FlaSH stack was incorporated as rear hole-selective contact in combination with a low-temperature-prepared SHJ front emitter in first demonstrator solar cells. With this proof-of-concept, p-type solar cells with conversion efficiencies up to 21.9% were reached with V$_{OC}$=698mV and FF=79.5%. These results clearly prove that our FlaSH technology represents a valid candidate for next generation of industrial and high-efficiency c-Si solar cells.

2. The FlaSH concept

Figure 1 describes the FlaSH concept applied to a p-type wafer along with its fabrication sequence. Central to FlaSH are a chemically-grown thin SiO$_x$ (<1.5 nm) capped with a boron-doped amorphous silicon carbide (a-SiC$_x$(p)) or alternatively an intrinsic amorphous silicon (a-Si(i))/SiC$_x$(p) bi-layer stack deposited by PECVD. Because of the fast ramps of the firing process (>50 °C/s), blistering of hydrogenated amorphous films is a common issue. As the film is heated to temperature >300 °C, hydrogen bonds rupture to form molecular hydrogen which

effuses from the layer. Especially with fast temperature ramps, hydrogen cannot effuse sufficiently fast but accumulates in the layer and eventually lifts the film off the substrate ("blistering"). Therefore, a first distinctive property of the thin-film materials the FlaSH concept relies on is resilience against blistering during the firing process. Another unique feature of our firing-compatible heterojunction is the good charge carrier selectivity even though the short thermal treatment is insufficient to diffuse a significant amount of dopants from the deposited doped layer into the wafer (see section 3.3), normally a condition that leads to poor charge carrier selectivity in existing poly-Si based passivating contacts[11,12,13,15,16,19]. To obtain thin-films with such unique characteristics we used PECVD, as this technique offers a multitude of possibilities to engineer the microstructural and electrical properties of the material. To prevent blistering, either the hydrogen content in the as-deposited film should be low, or the hydrogen bonding on the a-Si should be strengthened, such that it is released only at higher temperature. For this reason, we introduced C-atoms to the Si network, which improved the hydrogen bonding and thus shifted the H effusion to higher temperatures[20,21], enhancing the thermal stability of the film[22]. Additionally, SiC_x layers have the advantage of being chemically stable to the wet chemistry commonly used for c-Si solar cell processing. In "standard" diffused poly-Si based passivating contacts, surface passivation and charge carrier transport at the c-Si/SiO_x interface are promoted by a buried diffused junction with moderate doping concentration ($>10^{19}$ cm^{-3}) [11,12,13,15,16,19]. This region enables high-tunneling probability through the SiO_x, resulting from a better band edge alignment at the wafer surface (e.g. valence band for a hole selective contact) and at the heavily-doped poly-Si layer[19] (see Figure 2 (c)). It also provides an efficient surface passivation by field effect, as the density of minority carriers (e.g. electrons for a hole selective contact) and consequently their Shockley-Read-Hall (SRH) recombination rate is reduced without excessively increasing Auger recombination[19]. As the FlaSH cannot rely on the beneficial effects of the buried junction, (i) a low density of defects D_{it} at the c-Si/SiO_x interface, and (ii) a strong induced junction at wafer surface adjacent to the SiO_x are required to ensure surface passivation and charge carrier transport. To meet the first requirement, a SiO_x layer was grown on the wafer surface before deposition the SiC_x-doped layer. The SiO_x layer prevents epitaxial re-growth of the SiC_x layer during firing, which is beneficial because the interfaces of epitaxially regrown Si layers have a high defect density[23]. It also displaces structural defects within the deposited layer from the wafer/SiO_x interface without hindering charge carrier transport. Finally, the Si/SiO_x interface is beneficial because surface dangling bonds can be passivated by hydrogen resulting in very low D_{it}[24,25,26]. As the optimum temperature for hydrogenation passivation of the Si-SiO_x interface is in the range of 400°C to 500°C [26], (more details in ref. [16]), the temperature stability of the surface passivation is enhanced compared to a-Si(i):H. The second criterion can be fulfilled by inducing accumulation of holes (and repulsion of electrons) at Si-surface adjacent to the SiO_x (see Figure 2 (c)). To this aim, nano-crystalline silicon layers containing a small atomic fraction of carbon (nc-SiC_x(p)) were formed by partial crystallization during firing of highly-doped a-SiC_x(p):H that had been deposited by PECVD. Crystalline layers can accommodate a larger number of active dopants[27,28,29,30] compared to only amorphous layers. As result, a strong surface potential can be induced, which similarly to the buried diffused junction of a poly-Si passivating contact, promotes surface passivation and selective hole transport towards the c-Si/SiO_x interface.
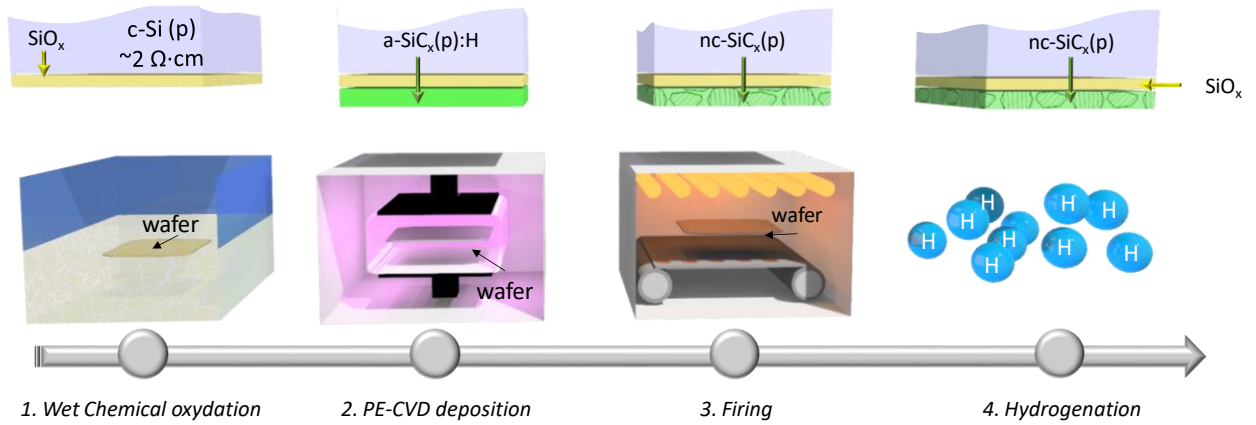
Figure 1. Fabrication steps of the FlaSH passivating contact. A thin (~1.4 nm) SiO_x is grown via chemical oxidation in hot HNO_3 (*step 1*). On top of that thin SiO_x layer a-SiC_x(p):H is deposited by means of PECVD (*step 2*). The layer stack is then fired in a rapid thermal annealing furnace (*step 3*), resulting in the transformation of the amorphous to a nano-crystalline silicon carbide (nc-SiC_x(p)) layer. Hydrogenation of the c-Si/SiO_x interface (see section methods) is finally employed (*step 4*).
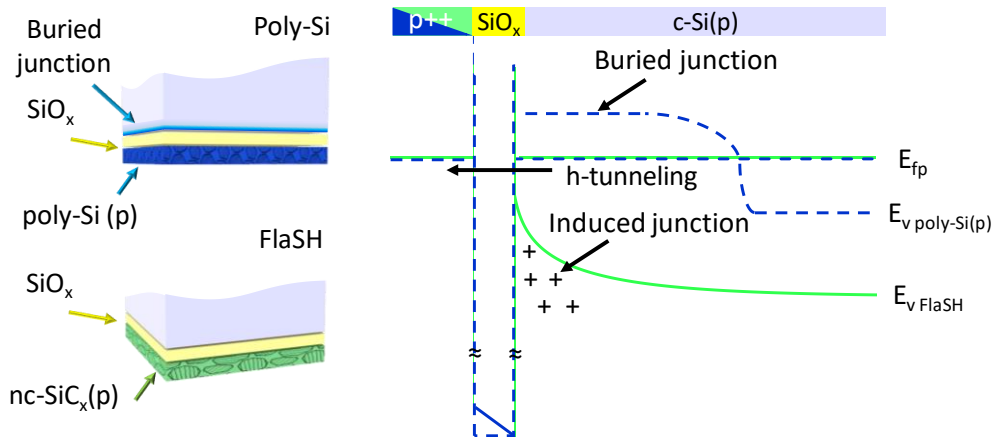

Figure 2. Valence band alignment of a poly-Si based passivating contact with buried junction and of the FlaSH concept based on an induced junction. In this example we assumed that the doping level of the buried junction makes the c-Si wafer a degenerate semiconductor. For simplicity same work functions for the applied hole-selective layers (poly-Si(p) and nc-SiCx(p)) are assumed.

3. Results and discussion

3.1 Evaluation of surface passivation and charge carrier transport

Effective minority carrier lifetime (τ_{eff}), implied open circuit voltage (i-V_{OC}) and dark saturation current density (J_0) measured by means of the photo-conductance decay method (PCD) were used to assess the surface passivation of the FlaSH hole selective junction. Figure 3(c) depicts τ_{eff} at an injection level of 10^{15} cm^{-3} (i.e. $\tau_{eff@10^{15}cm^{-3}}$) as a function of the normalized flow ratio (i.e. $CH_4/(H_2+CH_4+SiH_4+TMB)$) of the a-$SiC_x$(p):H deposited on both sides of chemically oxidized test structures (sketched in Figure 3 (a)). The figure reveals an increase of τ_{eff} as the normalized flow ratio decreases, until reaching an optimum value of 1100 µs. For this condition, an i-V_{OC} of 707 mV and J_0 of ~14 fA/cm^2 were measured. For lower normalized flow ratio, $\tau_{eff@10^{15}cm^{-3}}$ decreases again. The poor surface passivation obtained for C-rich layers (i.e. high flow-ratio) can be explained by an insufficient induced surface potential caused by several effects: lower doping efficiency[31,32], larger defect density[31], and retarded crystallization due to C-addition. Conversely, without incorporating carbon (i.e. normalized flow ratio equal to zero) the entire layer stack blistered during the fabrication sequence. This proves that C addition to the Si network is an essential feature of the FlaSH concept. As C-diffusion for the SiC_x(p) during firing can chemically
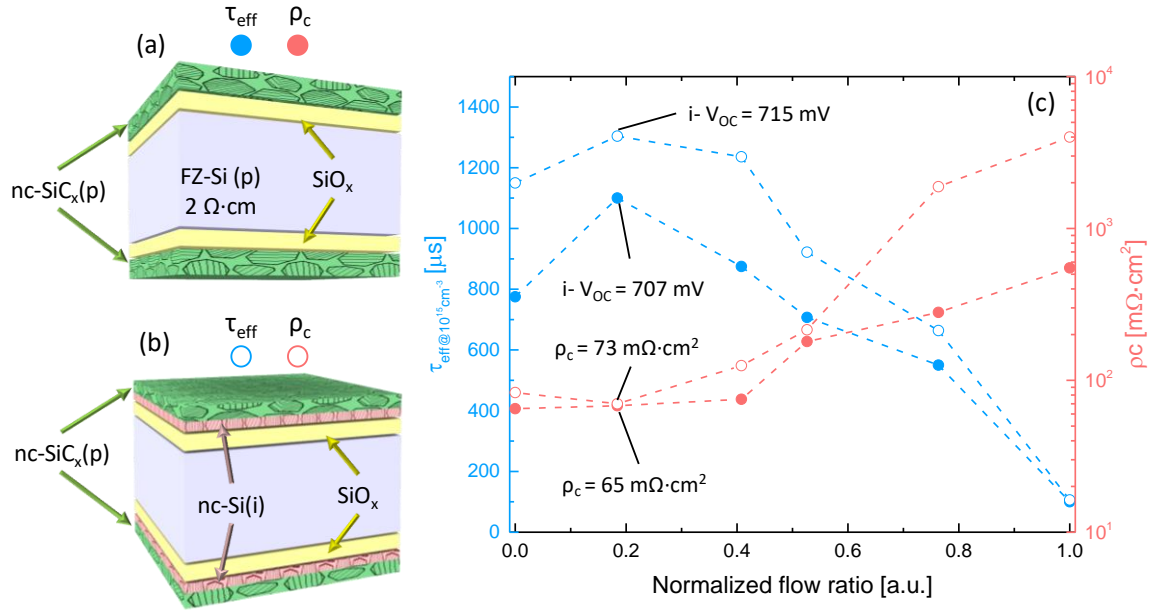
4

Figure 3. Effective minority carrier lifetime (τ_{eff}) at injection level of 10^{15} cm^{-3} (left axis) and contact resistivity (right axis) as a function of the normalized flow ratio (CH$_4$/(H$_2$+CH$_4$+SiH$_4$+TMB)) . Full symbols represent a single nc-SiC$_x$(p) layer as depicted in (a), open symbols represent nc-Si(i)/nc-SiC$_x$(p) bilayer structure as shown in (b). Total thickness for both layer stacks was kept constant.

react with oxygen from the SiO$_x$ and dissolve it[22], we replaced the first 10 nm of the SiC$_x$(p) layer with a-Si(i):H[22] as sketched in Figure **3** (b). As the a-Si(i) layer does not contain dopants, it also reduces the number of B-atoms diffusing through the SiO$_x$, an effect responsible for creating additional interfacial defects[33], thus acting as a dopant "buffer" layer (see section 3.3). As indicated by the improved i-V$_{OC}$ values in Figure **3**(c), the impact of the a-Si(i) buffer layer on the passivation quality becomes remarkable at low gas flow ratio, where the better doping efficiency in the nc-SiC$_x$(p) is expected to induce a stronger surface potential. Similarly as for the single FlaSH stack, without C-incorporation layer blistering was observed. For the bilayer stack we achieved an optimal in $\tau_{eff@10^{15}cm^{-3}}$ =1300 μs, i-V$_{OC}$ of 715mV and a J$_0$ of ~11 fA/cm^2 at normalized flow ratio of 0.18 (for the SiC$_x$(p)). The transport properties of the FlaSH passivating contact were evaluated by means of the contact resistivity (ρ_c) measured via transfer length method (TLM) after it with a sputtered ITO/Ag stack. The measured ρ_c strongly increased towards higher normalized flow ratio for both nc-SiC$_x$(p) and nc-Si(i)/nc- SiC$_x$(p) stacks, as reported Figure 3 (c). Interestingly, for low C-content, the additional nc-Si(i) buffer layer does not have a strong impact on ρ_c. This result could be related to the better doping efficiency in nc-SiC$_x$(p) with low carbon content which is capable of inducing hole conductivity in the nc-Si(i) buffer layer by the field effect, doping of nc-Si(i) as B diffused from the SiC$_x$(p) during firing. We obtained values of ρ_c of 65 mΩ·cm^2 and 73 mΩ·cm^2 for the nc-SiC$_x$(p) and nc-Si(i)/nc-SiC$_x$(p) (with normalized flow ratio of 0.18), respectively.

3.2 Proof-of-concept p-type solar cells employing the FlaSH contact as rear hole collector and conventional SHJ as front electron collector

The developed FlaSH passivating contact based on the single nc-SiC$_x$(p) or alternatively nc-Si(i)/nc-SiC$_x$(p) bilayer stack was applied as rear hole-selective contact in proof-of-concept solar cells with a standard SHJ at the front side. Since the front side processing not exceeding 200°C, it does not alter the properties of the FlaSH rear side and thus provides a suitable architecture to explore its junction properties. Figure 4 (a) and (b), report the *"hybrid"* solar cell structures employing the optimal (i.e. highest τ_{eff} and lowest ρ_c in Figure **3** (c)) single (nc-SiC$_x$(p)) and bilayer (nc-Si(i)/nc-SiC$_x$(p)) FlaSH stacks, respectively. Measured J-V characteristics and external parameters are reported in Figure 4 (c) and Table 1, respectively. V$_{OC}$ values of 698 and 706 mV were measured

for the hybrid cells employing the single and bi-layer FlaSH stacks. A V_{OC} loss of about 10 mV compared to the i-V_{OC} of the symmetrical test structures might be attributed to ITO sputtering induced damage and dark diode formation. The latter is related to the fact that both passivating contacts are deposited on the full wafer area and a black hard-mask ($2x2cm^2$) is used to define the cell area for the J-V measurements. The excellent charge carrier transport of the FlaSH are evidenced by fill factors above 78.5%. The hybrid cell employing the single stack exhibited lower V_{OC} but a higher FF compared to bilayer stack. This result is in good agreement with the i-V_{OC} and ρ_c trends reported in Figure **3** (c). Most likely, FF and J_{SC} values of such proof-of-concept solar cells are limited by parasitic absorption and charge carrier transport in the non-optimized SHJ.
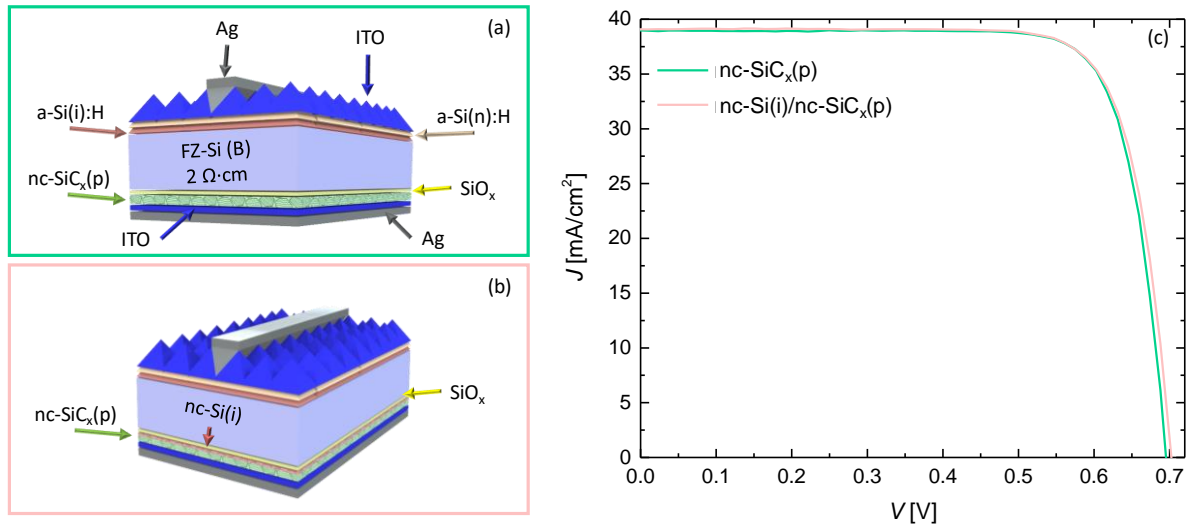

Figure 4. Sketch of the hybrid solar cell structure comprising a-Si(i):H/a-Si(n):H as front side emitter and the FlaSH rear hole selective contact formed by (a) nc-SiC$_x$(p) and (b) nc-Si(i)/nc-SiC$_x$(p) stack. The respective J-V characteristics are reported in (c) nc-SiC$_x$(p) (in green) and nc-Si(i)/nc-SiC$_x$(p) (in red).

	J$_{SC}$ [mA/cm^2]	V$_{OC}$ [mV]	FF [%]	η [%]	p-FF [%]
nc-SiC$_x$(p)	39.4	698	79.5	21.9	81.6
nc-Si(i)/nc-SiC$_x$(p)	39.3	706	78.3	21.7	81.8

Table 1. Summary of the solar cell performance parameters of the hybrid cells employing single (nc-SiC$_x$(B)) or bilayer (nc-Si(i)/nc-SiC$_x$(p)) configurations for the FlaSH rear hole selective contact.

3.3 SIMS analysis

The compositional profiles of the FlaSH contact were measured by secondary ion mass spectrometry (SIMS) analysis and are reported in Figure 5. Figure 4a reports the profile of the single nc-SiC$_x$(p), and Figure 4b the result for the bilayer nc-Si(i)/nc-SiC$_x$(p) FlaSH stacks, both in the as-deposited and fired states. The use of a low energy primary ion beam allowed us to rapidly reach equilibrium sputtering and ionization conditions on pristine surfaces. Thus, the variation of the signal intensity (*I*) of the measured species in the first few nanometers corresponds to native oxide and/or adsorption of species at the sample surface. The ions/elements here analyzed were B$^+$, C$^+$, O$^+$ and Si$^+$ (not reported here). The B signal was of primary interest to evaluate potential doping diffusion occurring during firing. The C signal was used to identify layer composition of the nc-SiC$_x$(p) and bilayer nc-Si(i)/nc-SiC$_x$(p) stack. The extent of the O peak was used to delineate the c-Si/SiO$_x$ wafer interface, indicated by a vertical yellow band in Figure 5 (a) and (d). Oxygen plays an important role in boron ionization efficiency (enhancement of B intensity with O presence). This results in an increase of B signal in SiO$_x$. As the magnitude of the oxygen peaks in the depth profiles obtained before and after firing, see Figure 5(c) and (f) and

the associated tables, show essentially no differences, hence, variations in the intensity of the B signal can be attributed to real variations in B concentrations. Starting from the sample with a single layer FlaSH stack, Figure 5(a) depicts a very abrupt B-profile in the c-Si for the as-deposited sample. Ideally a step function was expected but the interface is slightly enlarged due to the depth resolution of the SIMS measurement (about 4 nm). Hence, variation in the B-signal of more than 2 orders of magnitude within a depth below 5 nm cannot be resolved. Moreover, Figure 5(a) clearly indicates that the impact of firing on the depth profile of the B-signal in the c-Si is within 5 nm as for the as-deposited sample. Another consequence of firing, this time more visible in our measurements, is the B enrichment of the SiO_x layer or of its interface with the deposited layers. In particular, the B-peak in the SiO_x increases by a factor of 1.8 compared to the as-deposited state, see Figure 5(b) and the associated table. No substantial differences of the C-signals before and after firing were observed. SIMS measurements for the bilayer nc-Si(i)/nc-SiC$_x$(p) are reported in Figure 5 (d)-(f). As the figures show, the as-deposited sample also presents a fast decay of the B-signal in the c-Si, and the firing does not alter the depth of the B-signal in the wafer significantly. Clearly, after firing, the intensity of the B-signal in the nc-Si(i) layer increases compared to that of the as-deposited state, but does not reach the same level as in the nc-SiC$_x$(p). This could be explained by the lower total concentration of B-atoms for the nc-Si(i)/nc-SiC$_x$(p) compared to the nc-SiC$_x$(p) and to an insufficient B-diffusion in the nc-Si(i) because of the low thermal budget of the firing. As already observed for the single stack, B enrichment of the SiO_x occurs after firing. As the B-signal in the SiO_x is 3.8 times higher compared to the as-deposited state, see Figure 5(e) and the associated table, the relative magnitude of this effect is higher compared to the single FlaSH stack. Nevertheless, when comparing the absolute magnitude of B-peaks in the SiO_x, the single FlaSH stack shows a 1.5 times larger value with respect to the bilayer. This highlights the role of the a-Si(i) as part of the bilayer FlaSH stack in reducing B-enrichment of the SiO_x resulting in higher surface passivation quality.
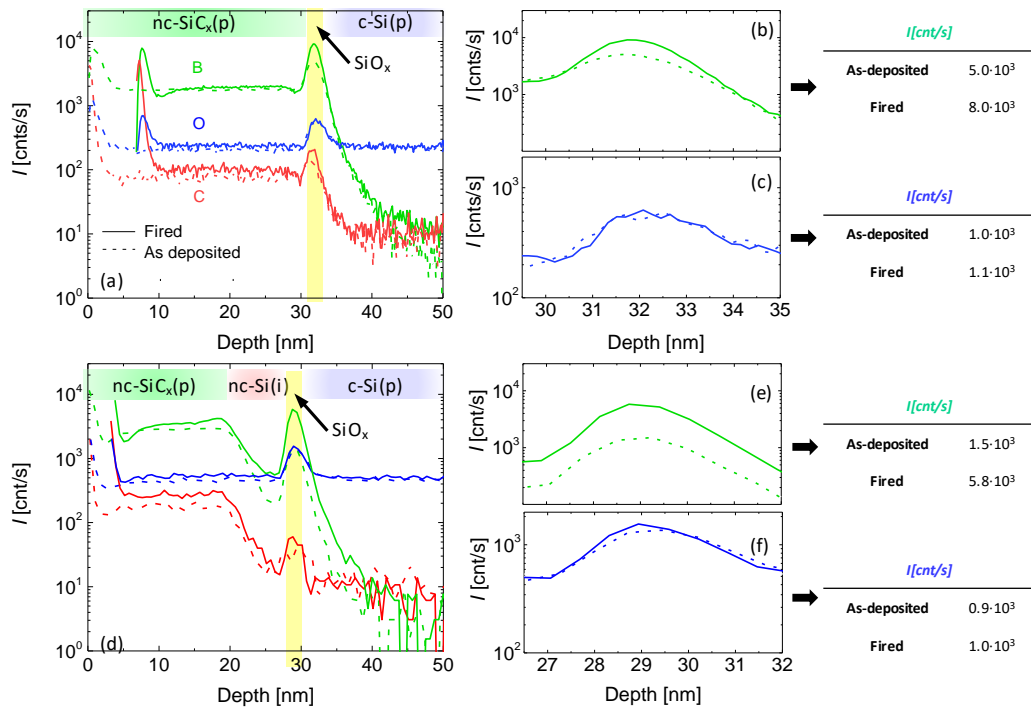

Figure 5. SIMS measurements of the FlaSH contact employing a SiC$_x$(p) with a normalized flow ratio of 0.18 (a) without and (d) with intrinsic buffer layer. The measurements are reported in in the as-deposited state and after firing steps. A magnification of the B and O signals are reported in the panels (b), (c) and (e), (f) for the single and bi-layer FlaSH contact. The tables summarize the intensity and area of the Gaussian curve used to fit the O and B peaks.

3.4 Microstructural investigation

The microstructure of the single and bi-layer FlaSH was investigated after firing by high resolution transmission electron microscopy (TEM). In all cases, the normalized flow ratio of the a-SiC$_x$(p) layers was set to 0.18. Scanning TEM images, which were acquired using a high-angle annular dark-field (HAADF) detector, are shown alongside energy-dispersive X-ray spectroscopy (EDX) maps for the two contact architectures in Figure **6** (a) and (b). These micrographs and chemical maps highlight clearly the 1 to 2 nm (in projection) passivating SiO$_x$ layer at the c-Si surface. In the case of the bi-layer stack, the evolution of the Si K, O K, and C K edge EDX intensities along the vertical axis make it possible to distinguish the start of the C-containing region ~7 nm from the c-Si surface (arrowhead in Figure 6 b). High-resolution TEM (HRTEM) images demonstrate a difference in crystallinity between the two contact architectures (Figure **6** c-d). The crystallinity of the nc-SiC$_x$(p) single layer stack appears homogenous, with no significant difference in the number of Si reflections observed in the Fourier transforms computed from the first part of the layer (the first ~7 nm near the SiO$_x$ buffer layer, inset i) or the rest of the layer (inset ii). On the other hand, Fourier transforms computed at the position of the intrinsic layer (the first 7 nm near the SiO$_x$ buffer layer, inset iii) shows more Si reflections than the Fourier transform taken at the position of the nc-SiC(p) layer (inset iv). As already observed in ref.[12], the presence of C appears to inhibit the crystallization of Si. In the case of the double layer nc-Si(i)/nc-SiC(p) stack (Figure **6** d), the presence of the underlying intrinsic layer may slightly increase the crystalline fraction in the upper boron-doped layer by promoting epitaxial growth of Si crystals across the interface nc-Si(i)/nc-SiC(p) during firing. Indeed, an inverse Fourier transform of the Si (111) reflection highlighted in green in Figure **6** d shows that large crystals spanning all the way across the two layers may form during firing, indicating that the crystallinity of the latter layer might be influenced by the presence of the underlying intrinsic layer. Overall, only Si reflections were indexed in the Fourier transforms of both contact structures. This indicates that the small amount of C is not sufficient to result in the formation of pure silicon carbide (SiC) crystals upon firing (C amount on the order of 2 at%, estimated using the Cliff-Lorimer method[34], a value influenced by C surface contamination in the microscope chamber). C hence ends up as a solid solute in the amorphous and nano-crystalline Si regions. It should also be mentioned that the use of shiny-etched wafers, which exhibit a small roughness, results in a slight blurring of the interfaces as these are observed in projection.
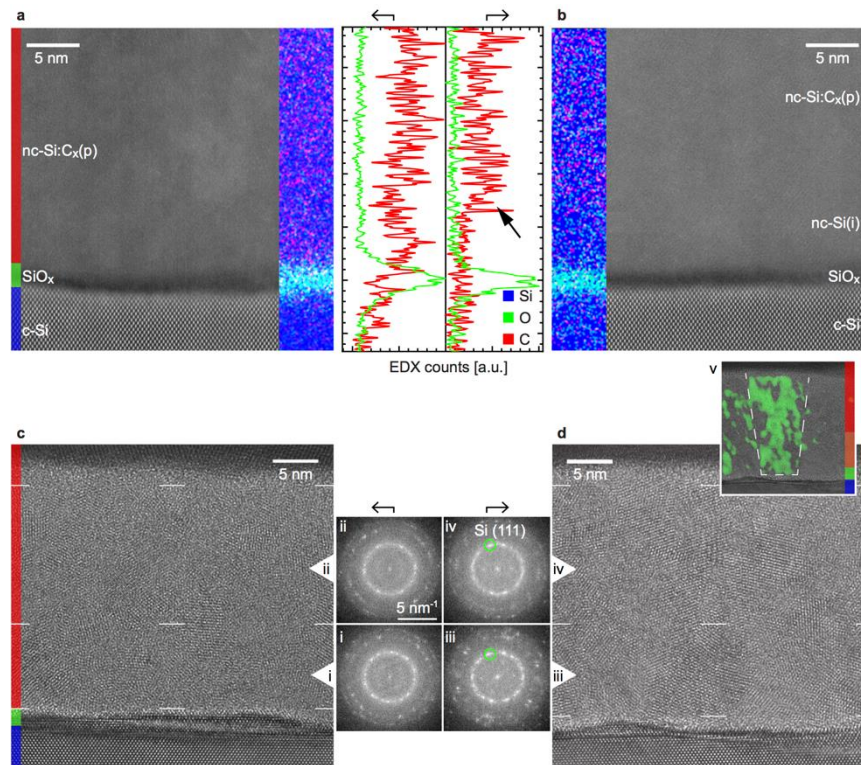

Figure 6. (a) STEM HAADF image of the c-Si/SiO$_x$/nc-SiC$_x$(p) contact, shown alongside an EDX map and a line scan of the Si K, O K, and C K edge EDX intensities. (b) STEM HAADF image and EDX map of the c-Si/SiO$_x$/nc-Si(i)/nc-SiC$_x$(p) double layer contact, also shown alongside the corresponding EDX line scan of the Si K, O K, and C K intensities. The arrow marks the position of the interface between the intrinsic and doped regions.

(c) HRTEM micrograph of the c-Si/SiO$_x$/nc-SiC$_x$(p) contact and corresponding Fourier transforms computed in the first 7 nm of the nc-SiC$_x$(p) close to the SiO$_x$ (inset i) and in the upper part of the doped layer (inset ii). (d) HRTEM micrograph the c-Si/SiO$_x$/nc-Si(i)/nc-SiC$_x$(p) double layer contact structure. Fourier transforms computed at the position of the intrinsic (inset iii) and doped (inset iv). An inverse Fourier transform of the Si (111) reflection highlights the presence of a large crystal spanning across the interface between the intrinsic and doped regions (inset v).

3.5 Micro-structural evolution of the FlaSH contact along the fabrication process

The micro-structural evolution and of the layers forming the FlaSH stack during the fabrication sequence was investigated by means of Fourier transform infrared spectroscopy (FTIR). We analyzed the FlaSH configuration based on the single a-SiC$_x$(p) with normalized flow ratio of 0.18 in the as-deposited, after firing and re-hydrogenation processes. The FTIR measurements depicted in Figure 7 (a) reveal the presence of various peaks. The first one is centered at 630 cm^{-1} and is associated to Si-H wagging or rocking modes[35,36] followed by the Si-C stretching mode[35,36] centered at 780 cm^{-1} while the Si-O stretching modes[37] appear at 1050 cm^{-1}. The band centered at 2050 cm^{-1} is attributed to Si-H$_n$ stretching modes[35] (with n=1, 2, 3). Finally, the absorption band between 2800 and 3000 cm^{-1} is associated to stretching modes of C-H$_n$ (n=1, 2, 3) groups in sp^2 and sp^3 orbital configurations[35]. The as-deposited sample (grey line) shows strong Si-H wagging and Si-H$_n$ stretching modes, which is typical of a-SiC$_x$:H layers. Additionally, a weak Si-C stretching mode and C-H$_n$ bands are observed. After firing (pink line), the spectrum shows the absence of all Si-H$_n$ modes, indicating that H bonded to Si effused out during firing. Interestingly, the C-H$_n$ stretching modes, which are more temperature stable[20], exhibit a reduced intensity compared to the as-deposited state but are still present. Additionally, a strong increase and a shift towards higher wavenumbers of the Si-C stretching mode is observed compared to the as-deposited state. This is a clear signature for the occurrence of a phase transition from a-SiC$_x$(p) to nc-SiC$_x$(p) state of the film[38,39,40,41] during firing. Moreover, the spectra show that the Si-O peak shifts towards higher wavenumber upon firing, which indicates the formation of a more stoichiometric film[37]. Interestingly, after the hydrogenation process(Figure 7 (a), blue line), the C-H$_n$ band again exhibits an intensity comparable to its intensity in the as-deposited state, proving that the hydrogenation process is effective in increasing the hydrogen content of the layer. We performed TDS measurements to analyze the hydrogen bonding more in detail. Mass separated ions (m/z) m/z=2 associated to desorption of H$_2^+$ are reported in Figure 7 (b). The as-deposited sample shows a broad H$_2^+$ effusion peak, which is commonly attributed to two effusion peaks, one at 220 °C (i.e. low temperature, LT) and one at 450 °C (i.e. high temperature, HT), appearing as a shoulder or plateau[42]. The LT peak is attributed to H$_2^+$ desorption due to simultaneous rupture of two Si-H bonds forming molecular hydrogen that effuses through internal voids or layer rupture[42]. The temperature of the LT peak is in agreement with literature data, as doped layers exhibit lower effusion temperature compared to intrinsic ones because the rupture of Si-H bonds is facilitated when the Fermi energy approaches the band egdes[37]. The HT peak is attributed to diffusion of mono-hydride (atomic hydrogen) through the layer network[42]. The presence of both peaks is explained by a reconfiguration of the internal Si-Si bonds, occurring during the heating process, transforming the network of voids, typical of SiC$_x$ layers, in a more compact network where diffusion of atomic H becomes the dominant mechanism of hydrogen transport, thus limiting the effusion rate. After firing at 800°C, H effusion from the nc-SiC$_x$(p) is, as expected, much lower compared to the as-deposited a-SiC$_x$(p):H (Figure 7 (b)). An increase in H$_2^+$ effusion is observed towards higher temperatures and could be associated to the rupture of the remaining C-H bonds (see FTIR measurements in Figure 7 (a)). The effusion spectrum of the hydrogenated sample shows a stronger H$_2^+$-effusion compared to the after firing state but lower than the as-deposited state. Additionally, a dramatic reduction of the H$_2^+$-effusion slope in the temperature range between 150 and 250°C, is observed for the hydrogenated and fired states compared to the as-deposited. This result might be explained by two mechanisms: 1) the more compact network of the nc-SiC$_x$(p) compared to the as deposited a-SiC$_x$(p):H reduces H-effusion; 2) hydrogen bonded at SiO$_x$/Si interface is thermally more stable compared to that of Si-H bonds that are typical of a-Si:H layers.
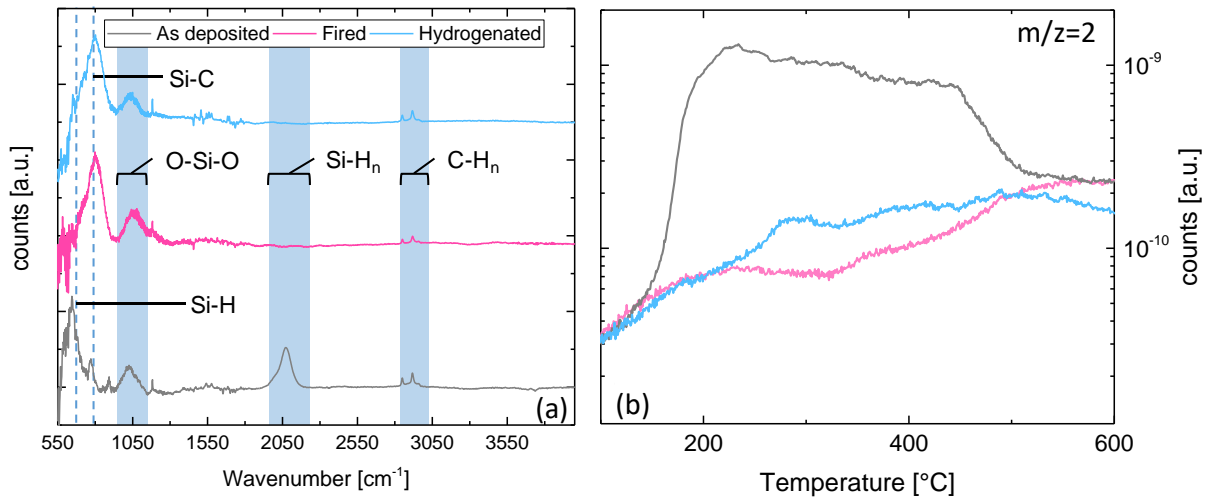
Figure 7. (a) FTIR measurements of the of the nc-SiC$_x$(p) with normalized flow ratio of 0.18 in the as deposited, fired and fired followed by hydrogenation. TDS measurements of (b) H$_2^+$-effusion spectra (m/z=2) of the SiC$_x$(B) with normalized flow ratio of 0.18 in the as-deposited, fired and hydrogenated states.

4. Outlook

4.1 Solar cell integration and efficiency potential

Industrial p-PERC solar cells are typically fabricated according to the topmost process sequence depicted in Figure 8. After texturing and cleaning of the wafer, an emitter is fabricated by phosphorous diffusion followed by a wet etching of the phosphorous silicate glass. A single side wet etching of the rear side is then applied to remove the P-diffused region and for surface planarization. For simplicity, this step is not reported in the fabrication sequence in Figure 8. A SiN$_x$:H layer is deposited by PECVD on the front surface serving as surface passivation and antireflection coating resulting in the cell precursor as depicted in *step 1* of Figure 8. Next, a dielectric layer (or stack of dielectrics) is deposited on the rear side, see *step 2,* and subsequently patterned as sketched in *step 3*. After screen-printing of Ag and Al pastes, respectively on the front and rear side of the cell (*steps 4 and 5*), a firing step is applied (*step 6*). Upon firing, the front Ag-based paste sinters through the SiN$_x$:H establishing a electrical contact with the underlying emitter, while on the rear side local Al-doped regions are formed (*step 6*). The bottom panel of Figure 8, depict the process flow of a solar cell with a diffused front emitter and the FlaSH full-area hole selective contact on the rear side. The process flow would begin by using the same cell precursor as for standard p-PERC (see *step 1*), with a selective emitter to take full benefit of the improved back-side. The growth of the thin SiO$_x$ can be performed during a cleaning step in hot HNO$_3$ after rear planarization. Afterwards, the SiC$_x$(p)-based layer can be deposited via PECVD on the rear side (*step 2.a*). Because the FlaSH contact combines the functionalities of passivation and charge carrier transport. Patterning of the rear contact is unnecessary. A Ag-based grid is then screen-printed on the front side (*step 3.a*) of the solar cell and fired through the SiN$_x$:H coating the front emitter. As result of the firing, an electrical contact between the Ag paste and the front emitter is established while on the rear side partial crystallization of the FlaSH contact takes place, as depicted in *step 4.a*. Hydrogenation is then carried out (see section methods) in order to enhance surface passivation (*step 5.a*) and alternatively can be integrated with the firing process. Finally, the rear side is metallized with a PVD stack of TCO (possibly In-free)/metal (possibly Al) (*step 6.a*). For this solar cell architecture, the application of a state-of-the-art front emitter metallized with screen-printing and firing-through (see for example[43]), would enable a conversion efficiency>23% with V$_{OC}$>700 mV, J$_{SC}$>41.5 mA/cm^2 and FF>81%, with strong upside potential for the FF.
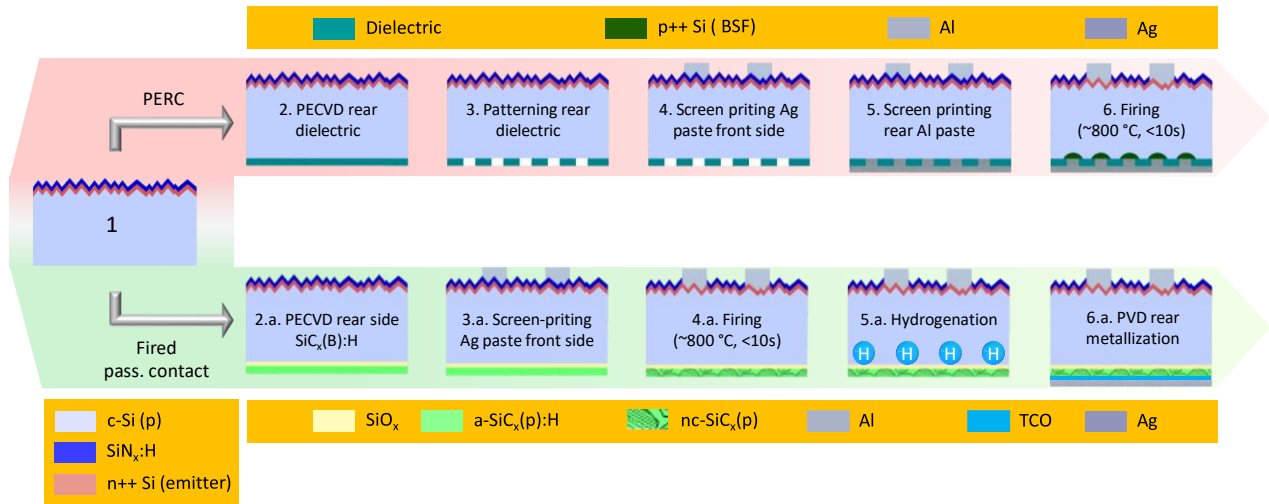
10

Figure 8. Process flow for manufacturing p-type PERC (*steps 1-6*) compared with one possible vision of FlaSH contact integration (*steps 1-6.a*).

5 Conclusions

In this work we demonstrated a firing-compatible silicon heterojunction (FlaSH) passivating contact aimed at resolving remaining challenges in industrialization of passivating contacts. Despite existing technologies employing long annealing steps, our FlaSH concepts is uniquely fabricated by means of firing that can be integrated with front side metallization formation. The addition of C to the Si network resulted of instrumental importance to minimize blistering effects by retarding H-effusion to higher temperatures. On symmetrically processes $iV_{OC} > 700$ mV and $\rho_c < 70$ $\Omega\cdot$cm^2 were obtained. By replacing part of the a-SiC$_x$(p) with an a-Si(i) layer iVoc was further boosted to 715 mV without dramatically affecting the transport properties of the junction. We identified as major cause for this effect, the reduction of B-enrichment of the SiO$_x$ upon firing, as the a-Si(i) acts as dopant buffer layer. Finally the integration of our stack into hybrid solar cells results in conversion efficiency up to 21.9% with V_{OC} above 700 mV and FF of 78.5%. The achieved results pave the way to a simplified co-fired step for the realization of a p-type solar cell with a full area rear passivating contact.

Acknowledgment

6 Methods

6.1 Fabrication of test structures for surface passivation and charge carrier transport

Boron doped float zone (FZ) 4-inch silicon planar wafers, (100) oriented, with thickness of 250 µm and resistivity ~2 $\Omega\cdot$cm were used for test structure fabrication. After cleaning using standard wet chemistry, a thin SiO$_x$ layer (~1.4 nm) was grown by wet chemical oxidation in hot nitric acid (69% w.t at 80 °C). Afterwards, a hydrogenated boron doped silicon carbide (a-SiC$_x$(B):H) or bilayer a-Si(i):H/a-SiC$_x$(B):H stacks were deposited via PECVD, at a temperature of 200 °C and a plasma frequency of 40.6 MHz on both sides of the wafer. The normalized flow ratio of the a-SiC$_x$(p):H (for single and bilayer configuration) was varied by changing the CH$_4$ gas-flow while keeping constant the other gas flows. A rapid thermal annealing process (RTP) based on fast ramps of 50 °C/s, peak temperature around 800 °C and dwell times in the order of 3 s, typical of industrial firing, was performed. All samples reported here were then hydrogenated by annealing of a hydrogen donor layer at 450 °C for 30 minutes. Such layer was then stripped by means of hydrofluoric acid. Coplanar ITO/Ag stack was sputtered on the FlaSH passivating contact through a hard metal mask in order to define the TLM patterning.

6.2 Solar cells

Hybrid c-Si solar cells employing conventional silicon heterojunction on the front side and the FlaSH hole selective contact on the rear side were fabricated. For such devices, we used same wafers as for the symmetrical test-structures described in Section 6.1. After

standard cleaning, front side surface texturing was performed by using a protective SiN_x:H layer on the rear side of the wafer, deposited by PECVD. After stripping of the sacrificial SiN_x, wafers were cleaned and chemically oxidized. PECVD deposition of the a-SiCx(p):H or alternatively a-Si(i)/SiC$_x$(p) was applied to the rear side of the cells followed by firing and hydrogenation (as discussed in the previous section). The front side heterojunction comprising of a-Si(i):H/a-Si(n):H stack was deposited by means of PECVD after a piranha cleaning of the solar cells. Finally transparent conductive oxide (ITO) was sputtered on both sides of the solar cells through aligned hard metal mask defining the cell area of 2x2 cm^2. Finally, a full area Ag blanket was sputtered on the rear side, while Ag metal fingers were screen printed on the front side.

6.3 Characterization

Minority carrier lifetime for the symmetrical samples was measured by using a Sinton WTC instrument. Dark saturation current densities were extracted by using the method of Kane Swanson. Solar cell I-V measurements were performed by using an AAA Wacom solar simulator calibrated with reference cells measured at CalLab PV Cells - Fraunhofer ISE.

Thermal desorption spectroscopy (TDS) was performed using an ESCO (EMD-WA1000S) system equipped with a quadrupole mass spectrometer. For the measurements, the base pressure of the chamber was set to 1×10^{-9} mbar, and samples of 1 cm x 1 cm were heated with a halogen lamp at a constant rate of 20°C/min up to 700°C. All the analyzed films were deposited on identical crystalline silicon substrates, including a reference sample for calibration of the system.

The SIMS depth profiles were obtained using a CAMECA SC-Ultra instrument with O_2^+ primary ions with 1 keV impact energy. Such low impact energy is needed to achieve very good depth resolution of the SIMS depth profiles. Although a setting with an even lower impact energy could be applied, this way was not chosen as sensitivity was preferred over depth resolution. The primary ion current was set to 2 nA. The ion beam was scanned over an area of 250 μm x 250 μm and the signal was acquired from inner area 60 μm in diameter. The acceptance energy window was 19 eV. The mass resolving power was set to 1200 in order to eliminate the contribution of $^{10}B^1H^+$ on $^{11}B^+$ signal. The secondary ions collected were: $^{11}B^+$, $^{12}C^+$, $^{16}O^+$ and $^{28}Si^+$ (not shown here). All the depth profiles were acquired with the same instrumental settings and analytical conditions such that the profiles can be compared directly. The depths of the SIMS sputtering craters were measured post-acquisition with a KLA-Tencor P17 profilometer. The sputtering time was converted to depth in nanometers assuming a linear erosion rate through the different layers. For a precise determination of the layer thicknesses, cross-section TEM images such as in Figure 6 is to be referred.

The microstructure of single and bi-layer contact stacks was assessed after firing using transmission electron microscopy. For that purpose, bulk samples were gold coated (to protect the contact) and cross-sections were extracted using the conventional focused ion beam lift-out method, which was performed in a Zeiss Nvision 40 workstation with a final Ga$^+$ voltage of 2 kV. In an image and probe Cs-corrected FEI Titan Themis microscope, STEM HAADF images were acquired in combination with EDX maps using a beam current of 200 pA at 200 kV. EDX spectra were quantified using the Cliff-Lorimer method implemented in the Bruker Esprit software [34]. In addition, high-resolution TEM micrographs were recorded. Fourier and inverse Fourier transforms of selected Si reflections were computed from these images using the software Digital Micrograph (Gatan, Pleasanton, USA) to assess the crystallinity of the layers.

FTIR we used a Nicolet 8700 FTIR spectrometer from Thermo (with a wheel sample holder to change between the reference wafer and the measured samples), with a beam splitter made of KBr and a DTGS detector. For typical measurements, we averaged over 32 scans and purged the setup with N2 for one night between inserting the sample and measuring to reduce artifacts from H2O and CO2. The setup is permanently purged with N2.

References

1.	International Energy Agency. *Market Report Series: Renewables 2017*. (IEA Publications).
2.	International Technology Roadmap for Photovoltaic (ITRPV). (2017).
3.	Marc, R., Steinkemper, H., Hermle, M. & Glunz, S. W. Numerical Current Density Loss Analysis of Solar Cell Concepts. **4,** 533–539 (2014).
4.	Ingenito, A., Isabella, O., Solntsev, S. & Zeman, M. Solar Energy Materials & Solar Cells Accurate opto-electrical modeling of multi-crystalline silicon wafer-based solar cells. *Sol. Energy Mater. Sol. Cells* **123,** 17–29 (2014).
5.	Cuevas, A. Physical model of back line-contact front-junction solar cells Physical model of back line-contact front-junction solar cells. *J. Appl. Phys.* **164502,** (2013).
6.	Yoshikawa, K. *et al.* Silicon heterojunction solar cell with interdigitated back contacts for a photoconversion efficiency over 26%. *Nat. Energy* **17032,** (2017).
7.	Pankove, J. I. & Tarng, M. L. Amorphous silicon as a passivant for crystalline silicon. *Appl. Phys. Lett.* **34,** 2–4 (1979).
8.	Wolf, S. De, Olibet, S. & Ballif, C. Stretched-exponential a - Si : H / c - Si interface recombination decay. *Appl. Phys. Lett.* **93,** 2–4 (2008).
9.	Hekmatshoar, B., Shahrjerdi, D., Hopstaken, M. & Sadana, D. Metastability of hydrogenated amorphous silicon passivation on crystalline silicon and implication to photovoltaic devices. *IEEE Int. Reliab. Phys. Symp. Proc.* 562–565 (2011). doi:10.1109/IRPS.2011.5784536

10. Yablonovitch, E. *et al.* A 720 mV open circuit voltage SiOx : c-Si : SiOx double heterostructure solar cell. *Appl. Phys. Lett.* 1211–1213 (1985).

11. F. Feldmann, M. Bivour. C. Reichel, M. Hermle, S. W. G. A passivated rear contact for high-efficiency. in (ed. Presented at the 28th European PV Solar Energy Conference and Exhibition, 30 September – 4 October, 2013, Paris, F.) (2013).

12. Römer, U. Polycrystalline silicon / monocrystalline silicon junctions and their application as passivated contacts for Si solar cells. *Dissertation* (2016).

13. Römer, U. *et al.* Solar Energy Materials & Solar Cells Recombination behavior and contact resistance of n þ and p þ poly-crystalline Si / mono-crystalline Si junctions. *Sol. Energy Mater. Sol. Cells* **131,** 85–91 (2014).

14. Haase, F. *et al.* Interdigitated back contact solar cells with polycrystalline silicon on oxide passivating contacts for both polarities. *Jpn. J. Appl. Phys.* **56,** 08MB15-1-5 (2017).

15. Yang, G., Ingenito, A., Hameren, N. Van, Isabella, O. & Zeman, M. Design and application of ion-implanted polySi passivating contacts for interdigitated back contact c-Si solar cells. *Appl. Phys. Lett.* **108,** 33903-1–4 (2016).

16. Nogay, G. *et al.* Solar Energy Materials and Solar Cells Interplay of annealing temperature and doping in hole selective rear contacts based on silicon-rich silicon-carbide thin fi lms. *Sol. Energy Mater. Sol. Cells* **173,** 18–24 (2017).

17. Young, D. L. Tunnel oxide passivated contacts formed by ion implantation for applications in silicon solar cells. *J. Appl. Phys.* **118,** 205701-1–9 (2015).

18. Richter, A., Benick, J., Feldmann, F., Fell, A., Hermle, M., Glunz, S. W. n-Type Si solar cells with passivating electron contact: Identifying sources for efficiency limitations by wafer thickness and resistivity variation. *Sol. Energy Mater. Sol. Cells* **173,** 96–105 (2017).

19. Steinkemper, H., Geisemeyer, I., Schubert, M. C., Warta, W. & Glunz, S. W. Temperature-Dependent Modeling of Silicon Solar Cells—Eg, ni, Recombination, and VOC. *IEEE J. Photovoltaics* **7,** 1–8 (2017).

20. Bullot, J. & Schmidt, M. P. Physics of Amorphous Silicon–Carbon Alloys. *Phys. stat. solid. B* **143,** 345–418 (1987).

21. Boccard, M. & Holman, Z. C. Amorphous silicon carbide passivating layers for crystalline-silicon-based heterojunction solar cells. *J. Appl. Phys.* **118,** (2015).

22. Nogay, G. *et al.* Silicon-Rich Silicon Carbide Hole-Selective Rear Contacts for Crystalline-Silicon-Based Solar Cells. *ACS Appl. Mater. Interfaces* **8,** 35660–35667 (2016).

23. Fujiwara, H. & Kondo, M. Impact of epitaxial growth at the heterointerface of a-Si:H/c-Si solar cells. *Appl. Phys. Lett.* **90,** 13503-1–3 (2007).

24. Cartier, E., Stathis, J. H. & Buchanan, D. A. Passivation and depassivation of silicon dangling bonds at the Si/SiO 2 interface by atomic hydrogen. *Appl. Phys. Lett.* **63,** 1510–1512 (1993).

25. Stesmans A. Interaction of P defects at the (111) Si/SiO2 interface with molecular b hydrogen: Simultaneous action of passivation and dissociation. *J. Appl. Phys.* **88,** 489–497 (2000).

26. Wilkinson, A. R. & Elliman, R. G. The effect of annealing environment on the luminescence of silicon nanocrystals in silica. *J. Appl. Phys.* **96,** 4018–4020 (2004).

27. Finger, F. *et al.* Improvement of grain size and deposition rate of microcrystalline silicon by use of very high frequency glow discharge. *Appl. Phys. Lett.* **65,** 2588–2590 (1994).

28. Imura, T. *et al.* Related content Evaluation of Boron and Phosphorus Doping Microcrystalline Silicon Films. *Jpn. J. Appl. Phys.* **23,** 549–551 (1984).

29. Seif, J. P. *et al.* Strategies for Doped Nanocrystalline Silicon Integration in Silicon Heterojunction Solar Cells. *IEEE J. Photovolt.* **6,** 1132–1140 (2016).

30. Nogay, G. *et al.* Nanocrystalline Silicon Carrier Collectors for Silicon Heterojunction Solar Cells and Impact on Low-Temperature Device Characteristics. *IEEE J. Photovolt* **6,** 1654–1662 (2016).

31. Stapinski, T., Ambrosone, G., Coscia, U., Giorgis, F. & Pirri, C. F. Defect characterization of a-SiC : H and a-SiN : H alloys produced by ultrahigh vacuum plasma enhanced chemical vapor deposition in different plasma conditions. *Phys. B* **254,** 99–106 (1998).

32. Anderson, D. A. & Spear, W. E. Electrical and optical properties of amorphous silicon carbide, silicon nitride and germanium carbide prepared by the glow discharge technique. *Philos. Mag. A J. Theor. Exp. Appl. Phys.* **35,** 1–16 (1977).

33. J. Snel. The doped Si/SiO2 interface. *Solid. State. Electron.* **24,** 135–139 (1981).

34. Cliff, G. & Lorimer, G. W. The quantitative analysis of thin specimens. *J. Microsc.* **103,** 203–207 (1975).

35. Saito, N., Tanaka, N. & Nakaaki, I. Optical, structural, electrical and optoelectronic properties of hydrogenated amorphous Si1–xC x alloy thin films prepared by planar magnetron sputtering method. *Appl. Phys. A* **38,** 37–43 (1985).

36. Demichelis, F., Giorgis, F., Pirri, C. F. & Tresso, E. Bonding structure and defects in wide band gap a-Si1–x C x :H films deposited in Hz diluted SiH4 + CH4 gas mixtures. *Philos. Mag. B* **71,** 1015–1033 (1995).

37. Pai, P. G., Chao, S. S., Takagi, Y. & Lucovsky, G. Infrared spectroscopic study of SiOx films produced by plasma enhanced chemical vapor deposition. *J. Vac. Sci. Technol. A* **4,** 689–694 (1986).
38. Janz, S. Amorphous Silicon Carbide for Photovoltaic Applications. 1–227 (2006).
39. Prado, R. Improvements on the local order of amorphous hydrogenated silicon carbide films. *J. Non. Cryst. Solids* **283,** 1–10 (2001).
40. Rovira, P. I. & Alvarez, F. Chemical (dis)order in a-Si1-xCx:H for x<0.6. *Phys. Rev. B* **55,** 4426–4434 (1997).
41. Rajagopalan, T. *et al.* Low temperature deposition of nanocrystalline silicon carbide films by plasma enhanced chemical vapor deposition and their structural and optical characterization. *J. Appl. Phys.* **94,** 5252–5260 (2003).
42. Beyer, W. Diffusion and evolution of hydrogen in hydrogenated amorphous and microcrystalline silicon. *Sol. Energy Mater. Sol. Cells* **78,** 235–267 (2003).
43. Deng, W. *et al.* 22 . 61 % Efficient fully Screen Printed PERC Solar. in *44th IEEE Photovoltaic Specialists Conference* (2017).